

```
\documentclass[a4paper, preprint]{revtex4-1}
\usepackage{amsmath}
\newcommand{\mean}[1]{\left\langle #1 \right\rangle}

\usepackage{graphicx}

\makeatletter
\renewcommand{\fnm@figure}{\figurename~S\thefigure}
\makeatother

\begin{document}
\title{Electronic Supplementary Information for ``Homogeneous melting near the superheat limit of hard-sphere crystals''}
\author{Feng Wang1, Ziren Wang2, Yi Peng1, Zhongyu Zheng{3,4}, and Yilong Han1}
\email{yilong@ust.hk}
\affiliation{1 Department of Physics, the Hong Kong University of Science and Technology, Clear Water Bay, Hong Kong, China\
2 Department of Physics, Chongqing University, Chongqing, China\
3 Institute of Mechanics, Chinese Academy of Sciences, Beijing, P.R.China\
4 University of Chinese Academy of Sciences, No.19\(A\) Yuquan Road, Shijingshan District, Beijing, 100049, P.R.China
}

\maketitle

\section{The Phase diagram of hard spheres}
The equilibrium and metastable phases of the 3D hard-sphere system are shown in Fig.~S\ref{fig:phase_diagram}. Hard spheres form a face-centered cubic (fcc) crystal at  $\phi > \phi_{\text{m}} = 0.545$ , a liquid phase at  $\phi < \phi_{\text{f}} = 0.494$ , and a coexistence of a  $\phi = 0.545$  crystal and a  $\phi = 0.494$  liquid between the melting point  $\phi_{\text{m}}$  and the freezing point  $\phi_{\text{f}}$ . A metastable supercooled liquid can form at  $\phi_{\text{f}} < \phi < \phi_{\text{g}}$  where the glass transition point  $\phi_{\text{g}} = 0.58$  can be regarded as the supercool limit. Superheated fcc crystals can form at  $\phi_{\text{limit}} < \phi < \phi_{\text{m}}$  where the superheat limit  $\phi_{\text{limit}} = 0.494 \pm 0.003$ . If spheres pack into an fcc lattice at  $\phi < \phi_{\text{s}} = 0.494$ , the crystal will collapse to a liquid state initiated by strong density fluctuations, i.e.  $\beta \leq 0$  and no energy cost is incurred for local volume changes.

\begin{figure}[!h]
\centering
\includegraphics[width=0.7\columnwidth]{figS1.pdf}
\caption{Phase diagram of hard spheres in 3D \cite{pusey_phase_1986, mulero_theory_2008}. The superheat limit is identified in the present work.}
```

```
\label{fig:phase_diagram}
\end{figure}
```

### \section{Order parameters}

The global translational order parameter  $Q_{\mathrm{T}}$ , the global orientational order parameter  $Q_{\mathrm{I}}$ , and the local orientational order parameters  $q_{\mathrm{I}}$  and  $\bar{q}_{\mathrm{I}}$  are defined as in the Materials and Methods of the main text and refs.~\cite{steinhardt\_bond-orientational\_1983, lechner\_accurate\_2008}. The decays of the order parameters  $Q_{\mathrm{T}}$ ,  $Q_{\{6,4\}}$  and  $\bar{q}_{\{6,4\}}$  can be fitted by the compressed exponential function  $Q(t) = (Q_{\mathrm{fcc}} - Q_{\mathrm{liquid}})e^{-(t/\tau)^\beta} + Q_{\mathrm{liquid}}$  (Figs.~2a-f of the main text). Liquid is disordered, hence its global orders  $Q_{\mathrm{T,6,4; liquid}} = 0$  as observed in Figs.~2a-c of the main text. Consequently,  $Q_{\mathrm{T,6,4}}(t) = Q_{\mathrm{T,6,4; fcc}}e^{-(t/\tau)^\beta}$ . Figure S\ref{fig:fit-all-order} shows that fitting different order parameters and pressure at each volume fraction yields the same  $\beta$  and  $\tau$ .  $\beta > 1$  in all simulations, indicating that the relaxation occurs at a higher rate than exponential.  $\beta \approx 2$  at  $\phi < 0.495$  and increases rapidly at  $\phi > 0.495$ . This might be related to the catastrophic melting at  $\phi < \phi_{\mathrm{limit}} = 0.494$  (Fig.~2h). Figure S\ref{fig:fit-all-L} shows the fitting parameter  $\beta$  of  $Q_{\mathrm{T}}(t)$  for 100 simulation trials with independent random initial velocities for each system size  $L = 4, 8, 16, 32, 64$ . It quantitatively shows that finite-size effect on the nucleation processes becomes negligible when  $L \geq 16$ .

```
\begin{figure}[!h]
\centering
\includegraphics[width=0.8\columnwidth]{figS2.pdf}
\caption{All order parameters and pressure in main text Fig.~2(a-f) yield the same fitted melting time  $\tau$  and exponent  $\beta$ . Symbols are from one trial of simulation used in Fig.~2a-f of the main text. Black curves are the average values of  $\tau$  and  $\beta$  from 100 independent simulations (Fig.~2g,h in the main text).}
\label{fig:fit-all-order}
\end{figure}
```

```
\begin{figure}[!h]
\centering
\includegraphics[width=0.6\columnwidth]{figS3.pdf}
\caption{The exponent  $\beta$  of the compressed exponential fits of  $Q_{\mathrm{T}}(t)$  from 100 independent simulations for system sizes  $L = 4, \sim 8, \sim 16, \sim 32, \sim 64$ .}
\label{fig:fit-all-L}
\end{figure}
```

```
\begin{figure}[!h]
\centering
\includegraphics[width=0.95\columnwidth]{figS4.pdf}
\caption{Orientational order parameters  $\langle w_6 \rangle$  and  $\langle w_4 \rangle$  with the
```

compressed exponential fittings (black curves) for crystals with  $4 \times 16^3$  hard spheres.  $\phi$  ranges from 0.47 (red) to 0.535 (blue) with a step size of 0.005. The fitted  $\tau$  and  $\beta$  have the same values as those fitted from other order parameters shown in Figs.~2g, h of the main text.

`\label{fig:fit-w}`  
`\end{figure}`

In addition to the order parameter shown in Fig.~2 of the main text, we also measured the order parameters [\cite{steinhardt\\_bond-orientational\\_1983}](#)

$$w_l(i) = \frac{\sum_{m_1+m_2+m_3=0} \begin{pmatrix} l & l & l \\ m_1 & m_2 & m_3 \end{pmatrix} q_{lm_1}(i) q_{lm_2}(i) q_{lm_3}(i)}{\left( \sum_{m=-l}^l |q_{lm}(i)|^2 \right)^{3/2}}$$

where  $\begin{pmatrix} l & l & l \\ m_1 & m_2 & m_3 \end{pmatrix}$  is the Wigner  $3j$  symbol.

$\langle w_l(i) \rangle$  is a rank-3 invariant of vector  $q_{lm}$ , representing the local  $l$ -folding orientational symmetry. They can also be well fitted by the compressed exponential functions (see Fig.~S\ref{fig:fit-w}).

`\begin{figure}[!h]`  
`\centering`  
`\includegraphics[width=0.7\columnwidth]{figS5.pdf}`  
`\caption{Order parameters of the hard-sphere fcc crystals. Crystals are stable at  $\phi > \phi_{\text{m}} = 0.545$ , metastable at  $\phi_{\text{limit}} = 0.494 < \phi < \phi_{\text{m}}$  and unstable at  $\phi < \phi_{\text{limit}}$ . The values for  $\phi > 0.5$  are obtained by averaging over the time interval  $[100\tau_0, 200\tau_0]$ . Crystals at  $\phi \leq 0.5$  are not stable during  $[100\tau_0, 200\tau_0]$ , hence we measured their values from the fitted  $Q_{\text{fcc}}$  in  $Q(t) = (Q_{\text{fcc}} - Q_{\text{liquid}}) \exp\left[-(t/\tau)^\beta\right] + Q_{\text{liquid}}$ , where the order parameters  $Q$  are shown in Figs.~2, S\ref{fig:fit-w}. The data points around  $\phi = 0.50$  from the two methods are smoothly connected, indicating that the two methods agree well and lends further confidence to the compressed exponential fittings. The solid lines are provided to guide the eye.}`  
`\label{fig:Qmean}`  
`\end{figure}`

Although the global order parameters  $Q_{\text{T}}$ ,  $Q_6$  and  $Q_4$  can hardly be directly measured near the superheat limit due to the limited lifetime of the crystal, they can be obtained from the compressed exponential fittings. Figure~S\ref{fig:Qmean} shows that they decrease as  $\phi$  decreases, but remain nonzero at the superheat limit, indicating that the behavior at the superheat limit does not resemble a critical behavior. In contrast to other order parameters, the local  $\langle q_4 \rangle$  and  $\langle w_4 \rangle$  in Fig.~S\ref{fig:Qmean} increase slightly at lower  $\phi$ , indicating a slight increase in local cubic ordering in deeply superheated crystals. Nevertheless,

this increase in local order disappears as soon as the order is coarse-grained by one more layer of nearest neighbors as shown by the  $\langle \bar{q}_4 \rangle$  curve in Fig.~\ref{fig:Qmean}. These coarse-grained order parameters  $\langle \bar{q}_4 \rangle$  and  $\langle \bar{q}_6 \rangle$  exhibit almost the same behavior as the corresponding global order parameters  $Q_4$  and  $Q_6$  (Fig.~\ref{fig:Qmean}), indicating that large fluctuations in deeply superheated crystals destroy the structural correlations beyond the nearest-neighbor length scale.

### Identification of crystal-like and liquid-like particles

We identify crystal-like and liquid-like particles using the traditional criterion of local order parameter \cite{gasser\_real-space\_2001, tan\_visualizing\_2014}. First, we identify the solid bond between neighboring particles  $i$  and  $j$  by the criterion  $\frac{\sum_m q_{6m}(i) q_{6m}(j)}{\sqrt{(\sum_m |q_{6m}(i)|^2)(\sum_m |q_{6m}(j)|^2)}} > 0.5$ . A particle is crystal-like if it possesses more than five solid bonds; otherwise it is liquid-like. Examples of liquid particles during the melting process are shown in Figs. 1a, c, e of the main text.

### Pressure and stress tensor

We calculate the stress tensor  $\sigma_{ij}$  and pressure  $P$  from the virial theorem by averaging over collision events in the event-driven molecular dynamics simulation,

\begin{equation}

$$\sigma_{ij} / \rho = -k_B T \delta_{ij} + \frac{m}{N \Delta t} \sum_{\alpha\beta} v_{\alpha\beta} r_{\alpha\beta, ij},$$

\end{equation}

and

\begin{equation}

$$P = -(\sigma_{xx} + \sigma_{yy} + \sigma_{zz})/3,$$

\end{equation}

where  $\rho$  is the number density;  $r_{\alpha\beta, ij}$  and  $v_{\alpha\beta, ij}$  are the  $i$ th spatial component (i.e.  $x, y, z$ ) of the relative position  $\mathbf{r}_{\alpha\beta}$  and velocity  $\mathbf{v}_{\alpha\beta}$  of the particle pair  $(\alpha, \beta)$ , respectively. The summation is taken over all pairs of particles  $(\alpha, \beta)$  colliding within a time interval  $\Delta t$ . A large  $\Delta t$  gives the time-averaged pressure, while a small  $\Delta t$  gives the instantaneous pressure. We chose  $\Delta t = 0.1 \tau_0$  for the instantaneous pressure  $P(t)$  during the melting, as shown in Fig.~2f of the main text.

To obtain the equation of state (EOS) and the time-averaged stress tensor for calculating elastic moduli, we averaged the order parameters over  $100 \tau_0$  to  $200 \tau_0$  for  $\phi > 0.50$  crystals, whose metastable state lasted long enough for statistics. At  $\phi \leq 0.50$ , the crystal becomes highly unstable with strong pressure fluctuations. Hence we measured  $P_{\text{fcc}}$  from the fitting of the instantaneous pressure  $P(t)$ ,

\begin{equation}

$$P(t) = (P_{\text{fcc}} - P_{\text{liquid}}) \exp\left[-(t/\tau_0)^\beta\right] + P_{\text{liquid}},$$

\label{eq:fitP}

\end{equation}

which is similar to the fitting of the order parameters. The fitting parameters  $P_{\text{liquid}}$  and  $P_{\text{fcc}}$  are the pressures of liquids and crystals, respectively. Our fitted pressures are

found to be well described by the Carnahan-Starling EOS  $\frac{\pi}{6} \frac{P}{\sigma^3} \frac{k_{\text{B}}T}{\sigma^3} = \frac{1 + \phi + \phi^2 - \phi^3}{(1 - \phi)^3}$  for liquid and our revised version of Speedy's EOS for crystal respectively (see Fig.~\ref{fig:EOS}). Note that the fitted  $P_{\text{fcc}}$  keeps decreasing even at  $\phi < \phi_{\text{limit}} = 0.494$ ; however, these values cannot be interpreted as the crystal's pressure because metastable crystals do not exist in this regime.

We found that Speedy's original EOS (with  $\zeta_1 = 0.620735$ ,  $\zeta_2 = 0.708194$  and  $\zeta_3 = 0.591663$  by fitting  $P$  at  $\phi \geq 0.52$  given by ref. \cite{bannerman\_thermodynamic\_2010}) cannot fit the bulk modulus  $B$  at low densities ( $\phi < 0.52$ ). Note that  $\frac{df}{d\phi} = \frac{d(f + \zeta_0)}{d\phi}$ , where  $\zeta_0$  is a constant. If we use the values  $\zeta_1 = 0.99 \pm 0.11$ ,  $\zeta_2 = 0.664 \pm 0.002$  and  $\zeta_3 = 0.645 \pm 0.003$  obtained by fitting  $B$ , and take  $\zeta_0 = P(\phi_{\text{m}}) - f(\phi_{\text{m}}) = 0.680$ , we can fit all measured values of pressure ranging from  $\phi = 0.494$  to  $0.6025$  well with no fitting parameter (Fig.~\ref{fig:EOS}). Hence the EOS for hard-sphere crystals should be revised to  $P = f + \zeta_0$  (where  $f$  is original Speedy's EOS with a revised  $\zeta_i$ ), which can fit a broad range of pressure and elastic modulus even in the deep superheating regime. The revision is also necessary since the original Speedy's EOS predicts the spinodal point to be at  $\phi = 0.471$ , which disagrees with our measured  $\phi_{\text{limit}} = 0.494$ .

```

\begin{figure}[!h]
\centering
\includegraphics[width=0.6\columnwidth]{figS6.pdf}
\caption{EOSs for hard-sphere liquids and fcc crystals. The measured pressures (blue squares) verify our revised version of Speedy's EOS (green curve) down to the superheat limit  $\phi_{\text{limit}} = 0.494$ . The parameters of revised EOS come from the fitting of Eqs. 2, 3 in the main text for the bulk modulus, and  $\zeta_0 = P(\phi_{\text{m}}) - f(\phi_{\text{m}}) = 0.680$ . Blue/black squares are time-averaged values for liquids; red and black dots represent values from compressed exponential fitting parameters  $P_{\text{fcc}}$  and  $P_{\text{liquid}}$  in Eq.~\ref{eq:fitP} respectively. Note that there is no free parameter for either of the curves describing the revised version of Speedy's equation and the Carnahan-Starling equation.}
\label{fig:EOS}
\end{figure}

```

### \section{Critical nucleus size predicted by the classical nucleation theory}

The classical nucleation theory (CNT) predicts the key parameters of nucleation processes, such as the critical nucleus size  $r^*$ , free energy barrier  $\Delta G^*$  and nucleation rate \cite{kalikmanov\_nucleation\_2013}. Generally, it applies well when the superheating or supercooling is weak. The CNT assumes that the nucleus is spherical with a radius  $r$ . Its excess free energy can be written as

```

\begin{equation}
\Delta G = - \frac{4}{3} \pi r^3 \rho \Delta \mu + 4 \pi r^2 \gamma + E_{\text{strain}},
\end{equation}

```

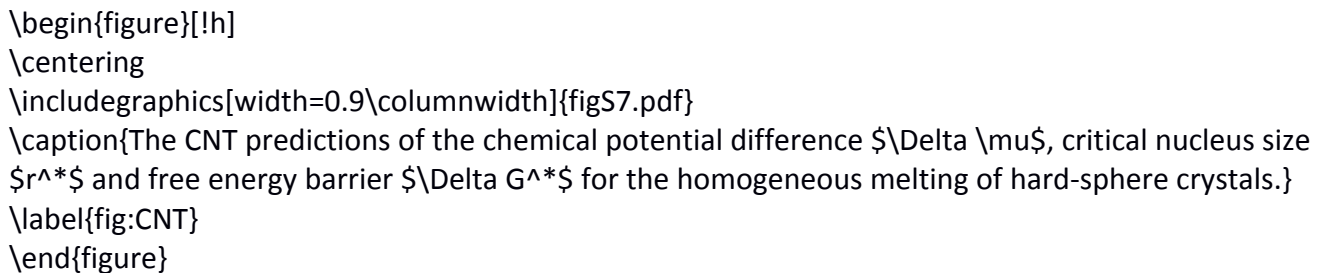
where  $\rho = \phi / (\pi \sigma^3 / 6)$  is the number density,  $\Delta \mu > 0$  is the chemical potential difference per particle between the metastable mother phase and the nucleus phase,  $\gamma$  is the interfacial energy between the two phases,  $E_{\text{strain}}$  is the possible

strain energy induced by elastic deformation when the parent phase is a solid.  $E_{\text{strain}}$  is usually negligible [cite{wang\_imaging\_2012}]. Here the parent crystal is assumed to have no preexisting defects so that there is no defect energy term in Eq.~5 [cite{wang\_melting\_2016}]. The competition of bulk and interfacial energy results into a nucleation barrier at the critical nucleus size  $r^* = \frac{2\gamma}{\Delta \mu \rho}$  and the nucleation barrier  $\Delta G^* = \frac{16\pi\gamma^3}{(\Delta \mu \rho)^2}$ .

The chemical potential per particle can be calculated in terms of the Gibbs-Duhem relation,  $d\mu = -sdT + \frac{dP}{\rho}$ , where  $s$  is the entropy per particle. Integrating along the isotherm line, we have  $\mu(\rho) = \int_{P_{\text{co}}}^{P(\rho)} \frac{dP}{\rho} + \mu_{\text{co}}$ , where  $P_{\text{co}}$  and  $\mu_{\text{co}}$  are the pressure and chemical potential at the coexistence phase. This formula works for both liquid and crystal, given the integral is along the corresponding EOS. Hence we have

$$\Delta \mu = \int_{P_{\text{co}}}^{P_{\text{crystal}}(\rho)} \frac{dP_{\text{crystal}}}{\rho} - \int_{P_{\text{co}}}^{P_{\text{crystal}}(\rho)} \frac{dP_{\text{liquid}}}{\rho}.$$

Using our revised Speedy's EOS for crystal and Carnahan-Starling EOS for liquid, the numerically calculate chemical potential difference is shown in Fig.~S\ref{fig:CNT}(a). Taking the liquid-crystal interfacial energy  $\gamma = 0.66 k_{\text{B}}T/\sigma^2$  for hard spheres [cite{hartel\_tension\_2012}], we obtain  $r^*(\phi)$  and  $\Delta G^*(\phi)$  as shown in Fig.~S\ref{fig:CNT}.



The predicted  $r^* < 7\sigma$  for  $\phi < 0.51$ . If non-CNT effects, such as coalescence of small nuclei or formation of precursors, are taken into account,  $r^*$  should be even smaller. Hence our system size  $L=16$  is large enough to study the homogeneous melting nucleation process at the strong superheat regime  $\phi < 0.51$ . Indeed, multiple liquid nuclei are observed at  $\phi=0.50$ , as shown in Fig.~1 of the main text and Movie 1.

In the  $NVT$  ensemble used in our simulations, the total volume is constant and the pressure changes during the melting process, see Fig.~2f in the main text. Hence, the density  $\rho$ , pressure  $P$  and the chemical potentials  $\mu_{\text{liquid}}$  and  $\mu_{\text{crystal}}$  are functions of the nucleus particle number. Nevertheless, if the critical nucleus radius  $r^*$  is much smaller than the system size, then the change of pressure before reaching  $r^*$  is negligible. Hence the nucleation in the  $NVT$  ensemble is identical to the one in the  $NPT$  ensemble. Therefore the finite-size effect

on nucleation in our  $\$NVT\$$  simulations is small.

### \section{Critical nucleus size estimated by the mean first passage time (MFPT) method}

The critical nucleus size can be estimated from the MFPT of the liquid nucleus size by assuming that the nucleation process can be described by the evolution of a single nucleus and the nucleation barrier is relatively high ( $\Delta G^* \gg k_B T$ ) \cite{wedekind\_new\_2007, lundrigan\_test\_2009}. The MFPT measures the average first time that the largest liquid nucleus  $n_{\max}$  in the superheated crystal reaches a given size. The MFPT of  $n_{\max}$  follows \cite{wedekind\_new\_2007},

\begin{equation}

$$\mathbf{MFPT}(n_{\max}) = \frac{1}{2JV} \left[ 1 + \mathbf{erf} \left( \frac{c(n_{\max}) - n^*}{\sqrt{2}} \right) \right],$$

\label{eq:mfpt}

\end{equation}

where  $\mathbf{erf}(x) = 2 \int_0^x e^{-x'^2} dx' / \sqrt{\pi}$  is the error function,  $n^*$  is the critical nucleus size,  $c = \sqrt{|\Delta G''(n^*)| / 2k_B T}$  is the local curvature at the top of the free energy barrier,  $J$  is the nucleation rate (number of nuclei per unit time and unit volume), and  $V$  is the volume of the system. The critical nucleus size corresponds to the location of the inflection point of the MFPT curve \cite{wedekind\_new\_2007}. Numerically, we performed the ensemble average over 100 independent simulation runs at each volume fraction  $\phi$ .

This method works well for estimating the critical nucleus size and the nucleation rate in the vapor condensation \cite{wedekind\_new\_2007} and crystallization in a weakly supercooled liquid \cite{lundrigan\_test\_2009}, where the nucleation is rare and dominated by the growth of the largest nucleus. At strong superheating, however, many nuclei grow simultaneously with frequent nuclei coalescence so that Eq.~\ref{eq:mfpt} cannot describe the nucleation process accurately. Furthermore, the critical nucleus is quite small under strong superheating, and any error induced by the definition of liquid-like particle could be comparable to the nucleus size, making the estimation inaccurate.

Nevertheless, we use the MFPT method to estimate the critical nucleus size to compare with our direct observation and the prediction from CNT in the last section.

\begin{figure}[!h]

\centering

\includegraphics[width=0.65\columnwidth]{figS\_mfpt.pdf}

\caption{(a) The MFPT (blue curve) of the largest liquid nucleus size  $n_{\max}$ , averaged from 100 independent simulation runs (gray curves), for  $\phi = 0.497, \sim 0.50, \sim 0.503$ . Red curves: the fittings of Eq.~\ref{eq:mfpt}. The critical nucleus sizes (green stars) correspond to the inflection points. (b) The fitted nucleation rate  $JV$ , critical nucleus size  $n^*$  and the critical nucleus radius  $r^*$  for various  $\phi$ 's.}

\label{fig:MFPTcritical}

\end{figure}

Each gray curve in Fig.~\ref{fig:MFPTcritical}a shows the first-passage time of the size of the largest liquid nucleus  $n_{\max}$  in an independent simulation run. We fit the average of them, the

$\mathrm{MFPT}(n_{\mathrm{max}})$ , by Eq.~\ref{eq:mfpt}, and the fitting parameters for  $\phi=0.50$  (middle panel of Fig.~\ref{fig:MFPTcritical}) give the critical nucleus size  $n^*=70\pm 0.5$ ,  $JV=(3.00\pm 0.01)\times 10^{-2}\tau_0^{-1}$ , or critical nucleus radius  $r^*=2.60\pm 0.006\sigma$ , and nucleation rate  $J=(1.7\pm 0.008)\times 10^{-6}\tau_0^{-1}\sigma^{-3}$ .

## Elastic constants

The elastic strain  $\epsilon_{ij}=\frac{1}{2}\left(\frac{\partial u_i(\mathbf{x})}{\partial x_j}+\frac{\partial u_j(\mathbf{x})}{\partial x_i}\right)$ , where  $i,j=x,y,z$  and  $u_i(\mathbf{x})$  is the displacement field at position  $\mathbf{x}$ .  $\epsilon_{ij}$  represents the  $j$ -direction gradient of the  $i$ th component of displacement \cite{landau\_theory\_2012}. Similarly, the stress tensor  $\sigma_{ij}$  measures the force gradient. Both  $\epsilon_{ij}$  and  $\sigma_{ij}$  are rank-2 symmetric tensors and have six independent elements for 3D crystals. The elastic constant  $C_{ijkl}$  is defined by the stress-strain relation  $\sigma_{ij}=\sum_{kl}C_{ijkl}\epsilon_{kl}+\sigma_{ij}^0$ , where  $\sigma_{ij}^0$  is the stress when no strain is applied. For a hard-sphere crystal,  $\sigma_{ij}^0$  is the negative pressure that is needed to hold the crystal together.  $C_{ijkl}$  is a rank-4 tensor with 36 independent elements for a general crystal. However, crystalline symmetries reduce this number greatly: a cubic crystal (e.g. fcc) has only three independent elements.

Voigt notation \cite{landau\_theory\_2012} is a simplified version of the elastic tensor notation. It maps  $ij$  pairs according to the rules:  $xx\to 1$ ,  $yy\to 2$ ,  $zz\to 3$ ,  $xy,yx\to 4$ ,  $xz,zx\to 5$  and  $yz,zy\to 6$ . Hence the stress-strain relation can be rewritten in a matrix-vector form,

$$\begin{aligned} & \begin{bmatrix} \sigma_1 \\ \sigma_2 \\ \sigma_3 \\ \sigma_4 \\ \sigma_5 \\ \sigma_6 \end{bmatrix} = \\ & \begin{bmatrix} C_{11} & C_{12} & C_{13} & C_{14} & C_{15} & C_{16} \\ C_{21} & C_{22} & C_{23} & C_{24} & C_{25} & C_{26} \\ C_{31} & C_{32} & C_{33} & C_{34} & C_{35} & C_{36} \\ C_{41} & C_{42} & C_{43} & C_{44} & C_{45} & C_{46} \\ C_{51} & C_{52} & C_{53} & C_{54} & C_{55} & C_{56} \\ C_{61} & C_{62} & C_{63} & C_{64} & C_{65} & C_{66} \end{bmatrix} \\ & \begin{bmatrix} \epsilon_1 \\ \epsilon_2 \\ \epsilon_3 \\ \epsilon_4 \\ \epsilon_5 \\ \epsilon_6 \end{bmatrix} \end{aligned}$$

```

\epsilon_6 \\
\end{array}\right]+
\left[\begin{array}{c}
\sigma_1^0 \\
\sigma_2^0 \\
\sigma_3^0 \\
\sigma_4^0 \\
\sigma_5^0 \\
\sigma_6^0
\end{array}\right].
\end{equation}

```

The symmetry of a cubic crystal simplifies the elastic tensor to

```

\begin{equation}
C=\left[\begin{array}{cccccc}
C_{11} & C_{12} & C_{12} & 0 & 0 & 0 \\
C_{12} & C_{11} & C_{12} & 0 & 0 & 0 \\
C_{12} & C_{12} & C_{11} & 0 & 0 & 0 \\
0 & 0 & 0 & C_{44} & 0 & 0 \\
0 & 0 & 0 & 0 & C_{44} & 0 \\
0 & 0 & 0 & 0 & 0 & C_{44}
\end{array}\right].
\end{equation}

```

Here the elastic constants are calculated according to the stress-strain relation [cite{frenkel\\_elastic\\_1987}](#). We applied a uniaxial strain  $-0.01 < \epsilon_{xx} < 0.01$  and measured the corresponding stress  $\sigma_{xx}$  and  $(\sigma_{yy} + \sigma_{zz})/2$  to obtain the elastic constants  $C_{11}$  and  $C_{12}$  (see [Figs.~S\ref{fig:stress-strain}a, b](#)). The bulk modulus  $B=(C_{11}+2C_{12})/3$ . The shear modulus  $C'=(C_{11}-C_{12})/2$ . We also applied a shear strain  $-0.01 < \epsilon_{xy} < 0.01$  and measured  $\sigma_{xy}$  to obtain the shear modulus  $C_{44}$  shown in [Fig.~S\ref{fig:stress-strain}c](#).

```

\begin{figure}[!h]
\centering
\includegraphics[width=0.95\columnwidth]{figS8.pdf}
\caption{Stress-strain relations of hard-sphere crystals. (a)  $\sigma_{xx}$ - $\epsilon_{xx}$ . (b)  $(\sigma_{yy} + \sigma_{zz})/2$ - $\epsilon_{xx}$ . (c)  $\sigma_{xy}$ - $\epsilon_{xy}$ .  $\phi$  ranges from 0.51 (top, red) to 0.6025 (bottom, blue), with a step size of 0.025. The slopes are used to calculate the corresponding elastic constants  $C_{11}$ ,  $C_{12}$  and  $C_{44}$ . The bulk modulus  $B=(C_{11}+2C_{12})/3$ . The shear modulus  $C'=(C_{11}-C_{12})/2$ . The intercepts at  $\epsilon_{xx}=0$  in (a, b) are equal to  $-P$ , where  $P$  is the pressure.}
\label{fig:stress-strain}
\end{figure}

```

In [Fig.~3b](#) of the main text, we extrapolate elastic moduli to zero in the low density regime using Eqs. 2, 3 in the main text based on Speedy's EOS. This functional form makes the fitting more physical than polynomial fits and captures both the divergence at the closest packing  $\phi_{\text{cp}}=0.7405$  and the trend in the low density regime. We used an iterative approach to fit the data: (1) Fix  $C_{44}$  at

a reasonable value to capture the asymptotic behavior at  $\phi \rightarrow \phi_{\text{cp}}$ , and fit the data to obtain  $c_1$ ,  $c_2$  and  $c_3$ ; (2) fix  $c_1$ ,  $c_2$  and  $c_3$ , and obtain  $c_4$  by fitting the data again; and (3) repeat steps 1 and 2 multiple times until  $c_{1,2,3,4}$  converge. This approach not only enables a close fitting of all three elastic moduli over the whole range of  $\phi$  (Fig. 3b), but also yields the right asymptotic divergence coefficient  $c_4$  at  $\phi_{\text{cp}}$ .

Figure~\ref{fig:polyfit} shows that polynomial extrapolations typically used in the literature fail to identify the correct superheat limit. The quadratic extrapolations in Fig.~\ref{fig:polyfit}a do not fit the data well and do not reveal the vanishing points of elastic moduli. Both the cubic polynomial and Speedy's EOS have four fitting parameters and can well fit the measured data (Fig.~\ref{fig:polyfit}b and Fig.~3b) for the middle range of  $\phi$ . However, the cubic extrapolation cannot reproduce the divergence of the elastic moduli at  $\phi_{\text{cp}}$  as Speedy's EOS does, since polynomial is not divergent at any finite  $\phi$ . More importantly, the cubic polynomial shows that the first instability occurs at  $\phi=0.485$  ( $C'=0$ ), which disagrees with the observed instability in the range  $0.49 < \phi < 0.495$  in Figs.~2, 5d of the main text. Hence Eqs. 2, 3 in the main text should be more reliable as the extrapolation functional form for elastic moduli than the cubic form.

```

\begin{figure}[!h]
\centering
\includegraphics[width=0.95\columnwidth]{figS9.pdf}
\caption{Elastic moduli extrapolated to zero using (a) quadratic and (b) cubic fittings.}
\label{fig:polyfit}
\end{figure}

```

\section{Movies}

Movie 1:\\

The melting process in real space, which corresponds to Figs.~1a, c, e of the main text. Crystal-like particles are shown as small blue dots. Liquid-like particles are colored according to their local order  $\bar{q}_6$  from 0.3 (blue) to 0.1 (red).

Movie 2:\\

The evolution of particles' order parameters  $\bar{q}_6$  and  $\bar{q}_4$  during the melting in Movie 1, which corresponds to Figs.~1b, d, f. The labels of ``bcc'', ``hcp'' and ``fcc'' denote the positions of these perfect lattices in the  $\bar{q}_6$ - $\bar{q}_4$  plane. The intensity of the color represents the logarithm of the statistical counts.

```

\bibliographystyle{apsrev4-1}

```

```

\bibliography{HSmelt}

```

```

\end{document}

```